nature communications

Article

https://doi.org/10.1038/s41467-025-65579-1

Cross-scale high-bandwidth atomic force microscopy with a stick-slip nanopositioner

Received: 19 November 2024

Accepted: 17 October 2025

Published online: 26 November 2025

Check for updates

Xiangyuan Wang[1], Qi Yu[1], Yixuan Meng[1], Jing Wang[1], Hu Huang[2] & Limin Zhu[1,3]

The core of atomic force microscopy (AFM) lies in the ultra-precise scanning between the tip and sample, which is enabled by nanopositioners. State-of-the-art AFMs generate the scanning motion using direct-drive nanopositioners, possessing either long range or high bandwidth, but not both. Here we show that with a triple-phase controller, the high-bandwidth (up to 363 Hz) nano-precision scanning can also be performed with a typical stick-slip nanopositioner. More importantly, by leveraging the displacement accumulation in the stepping mode, the same system achieved a 3 mm × 3 mm *XY* working range, 1-2 orders of magnitude larger than those direct-drive nanopositioners with a similar bandwidth. We further developed a versatile stick-slip AFM and demonstrated high-line-rate AFM imaging at 40 Hz over millimeter-scale areas. This work expands the functional scope of stick-slip nanopositioners, traditionally limited to static nanopositioning or long-range coarse positioning, and offers a cross-scale, high-bandwidth solution for next-generation AFMs.

Atomic force microscopy (AFM) is a powerful multifunctional platform that enables the exploration of electron spin[1], mechanobiology[2], and more by nanometer-scale measurement[3]. With the rapid advances in materials science[4], biophysics[5], and the semiconductor industry[6], observing large objects with high efficiency is now demanding. In particular, next-generation AFMs require simultaneous nanometer precision, long motion range, and high bandwidth. Such challenging requirements could only be resolved by enhancing nanopositioning performance, which is enabled by the core of AFM: the nanopositioners[7].

The nanopositioners generate ultra-precise scanning motion between the AFM probe tip and the sample[7]. Currently, direct-drive nanopositioners have become the standard in state-of-the-art AFMs, owing to their friction-free transmission characteristics[8]. However, according to Hooke's law and Lagrangian mechanics, direct-drive nanopositioners face a fundamental trade-off between the scanning range and the resonance frequency (the resonance frequency dominates the operation bandwidth)[8]. High-stiffness direct-drive systems perform a high resonance frequency but are limited in range, and vice versa (Fig. 1a). To fulfill different performance demands, a range of actuation technologies has been explored. Among them, piezoelectric-actuated systems are the most widely used. They leverage the high stiffness and fast response of the piezoelectric actuator to achieve a high bandwidth[8,9]. However, their working range is limited (typically no more than 100 µm) by the low strain (about 0.1%) of piezoelectric ceramics[10,11]. Voice coil-actuated nanopositioners offer a long range (typically longer than 1 mm), but suffer from low structural stiffness, resulting in resonances at tens of Hertz and restricting scanning frequencies to below 2 Hz[12,13]. Normal-stressed electromagnetic actuators have been proposed as a compromise, yet their performance remains intermediate[14,15]. Achieving both long-range and high-bandwidth in a single nanopositioning system remains an unresolved challenge.

Stick-slip nanopositioners can offer macro-scale long motion ranges (typically >1 mm) by incrementally accumulating displacements in the stepping mode[16], and fast response by the piezoelectric actuation[17]. Despite these advantages, they have long been considered unsuitable for nano-precision applications such as AFM scanning, mainly due to the frictional relationship between the compliant mechanism and the slider. Kinetic friction happens between successive steps, leading to backward motion effect[18]. This effect introduces uncertainties in the step size Δ_{step} on the order of tens of nanometers

[1]State Key Laboratory of Mechanical System and Vibration, School of Mechanical Engineering, Shanghai Jiao Tong University, Shanghai, China. [2]Key Laboratory of CNC Equipment Reliability, Ministry of Education, School of Mechanical and Aerospace Engineering, Jilin University, Changchun, China. [3]The Shanghai Key Laboratory of Networked Manufacturing and Enterprise Information, Shanghai, China. e-mail: zhulm@sjtu.edu.cn

(Fig. 1b)[19]. Although some AFM systems incorporate stick-slip stages, they are typically used only for coarse positioning in dual-stage architectures, while the fine scanning motion is still delegated to a direct-drive nanopositioner[20]. Over the past decade, both industrial and academic communities have explored the feasibility of operating stick-slip nanopositioners in a mode free from kinetic friction, i.e., the scanning mode, to enhance resolution[18]. However, such demonstrations have so far been restricted to quasi-static conditions, such as holding position or scanning at very low frequencies[21,22]. Hitherto, it is still unclear whether stick-slip nanopositioners can support long-range, nano-precision, dynamic scenarios such as cross-scale high-bandwidth AFM.

In this work, we demonstrate an AFM system that simultaneously achieves nanometer-level repeatability, long-range motion (>3 mm), and high-bandwidth scanning (up to 363 Hz), all powered by a single stick-slip piezoelectric nanopositioner. This is enabled by a triple-phase control scheme. In phase-1, the system is excited at the optimal frequency to achieve high-velocity stepping (26.8 mm/s along *X*-axis, 23.1 mm/s along *Y*-axis) over a 3 mm × 3 mm working area, which is 1-2 orders of magnitude larger than the range of typical piezoelectric direct-drive nanopositioners. Phase-2 employs a wrap-state integral controller to enable seamless transitions between the scanning and stepping modes. Phase-3 introduces a damping-tracking feedback controller, allowing a high control bandwidth near the mechanical resonance frequency, delivering excellent raster scanning capability comparable to that of direct-drive piezoelectric stages. The integration of these control phases bridged the gap between high-velocity stepping and high-bandwidth scanning, enabling cross-scale-level (from nano to macro) versatility. We further integrated the stick-slip nanopositioning system with a commercial AFM head, and carried out cross-scale high-bandwidth sampling imaging and stitching imaging over millimeter-scale areas. These results show that, with appropriate control, a typical stick-slip nanopositioner can meet the precision and bandwidth demands of AFM while offering an extended range — challenging the long-standing view that AFM scanning can only be achieved by direct-drive nanopositioners. This work not only expands the functional scope of stick-slip nanopositioners, but also offers a cross-scale, high-bandwidth solution for next-generation AFMs.

Results

Structure and working principle of the stick-slip AFM nanopositioner

In three degrees of freedom nanopositioning applications, such as AFMs, long-range scanning along the *X*- and *Y*- axis is always desirable, ideally at the macro scale[23,24]. While the scanning along the *Z*-axis is generally at the micro scale, considering the height of the surface topography. Here, we present a three degrees of freedom system to move the sample relative to an AFM probe (Fig. 1c).

In particular, the system consists of *Z*-, *X*-, and *Y*-stages arranged in series from top to bottom. To enable the positioning from nano to macro scale, the *X*- and *Y*- stages adopt the stick-slip principle, with structural designs modified from our previously reported configuration[25]. Each stage comprises a piezoelectric stack, a compliant mechanism with a lever (Supplementary Fig. 1), a slider, and the connection parts (Fig. 1c). The slider is connected to the compliant mechanism via a frictional interface. The compliant mechanism incorporates a long, low-stiffness cantilever at the output to mitigate the influence of assembly variations and mechanical wear on performance[25]. Titanium alloy TC4 is used for the compliant mechanism to enhance the wear resistance compared to commonly-used aluminum-based mechanisms. The *X*- and *Y*- stages are identical in structural configuration and parameters (Supplementary Fig. 1), except for minor differences between their bases. The *Z*-axial direct-drive stage consists of a piezoelectric stack, a compliant mechanism (Supplementary Fig. 2), and a wedge for the provision of preload, allowing precise tracking of the micro surface topography (height variation) by keeping the tip-sample interaction constant, which is monitored by an embedded AFM sensing system with a laser beam, a probe, and a photodiode. The effectiveness of the compliant mechanisms was demonstrated via finite element simulation (Supplementary Figs. 1 and 2).

Stick-slip nanopositioners operate in two modes: stepping and scanning. In the stepping mode, periodical sawtooth signals are employed to excite the piezoelectric stack, enabling a long-range coarse motion (Fig. 1d)[26]. Each period T of the sawtooth signal comprises a loading stage and an unloading stage. The moments of the start, the maximum value, and the end of a period were labeled as moment-1, moment-2, and moment-3, respectively. From moment-1 to moment-2 (the stick stage), the piezoelectric stack gradually elongates in response to the increasing voltage, thereby exerting force on the compliant mechanism and driving its deformation. Concurrently, the slider travels a distance Δ as a consequence of the static friction between the slider and the compliant mechanism. Between moment-2 and moment-3 (the slip stage), the excitation voltage drops suddenly, causing the compliant mechanism to return rapidly to its initial position as the piezoelectric stack retracts abruptly. Owing to the inertia, the slider tends to maintain its position through relative slipping between the slider and the compliant mechanism[19,26]. However, kinetic friction during this slipping motion induces a small backward displacement, i.e., the so-called backward motion effect (Fig. 1b), resulting in a net step size Δ_{step} that is slightly smaller than Δ (Fig. 1d)[27]. By repeating the sawtooth excitation, a macro-scale motion range can be achieved via displacement accumulation[9,16]. The stepping velocity can be optimized by tuning the excitation amplitude and frequency, and the motion direction can also be reversed by inverting the sawtooth signal[28,29]. To note, friction-induced backward motion between successive steps introduces uncertainties on the order of several tens of nanometers per step, which accumulate progressively with each step. As a result, nanometer-level precision is fundamentally unachievable in the stepping mode alone.

In the scanning mode, the piezoelectric stack is excited by waveforms with relatively low acceleration—such as triangular or sinusoidal signals—insufficient to overcome the static friction. In this regime, the slider remains fully stuck with the compliant mechanism throughout the cycle, eliminating kinetic friction and thus enabling nanometer-scale resolution (Fig. 1e)[22,30]. As the slider always sticks with the compliant mechanism, the stick-slip nanopositioner in the scanning mode behaves like a direct-drive system, and the pure scanning range is at the micro scale.

These two modes offer complementary capabilities: Stepping mode provides a macro-scale range but suffers from friction-induced uncertainty. While scanning mode offers nanometer precision but has a small pure scanning range. To bridge these regimes and achieve cross-scale versatility, we introduce a triple-phase control strategy (Supplementary Fig. 3). It includes phase-1 for maximizing the velocity in the stepping mode, phase-2 for the seamless transition between the two modes, and phase-3 for enhancing the control bandwidth in the scanning mode. The following two sections will present details and advanced functions of phase-1 and -2, followed by those of phase-3.

Seamless transition between stepping and scanning enables cross-scale nanopositioning and tracking

Integrating the stepping and scanning motion effectively is the key for stick-slip nanopositioners to achieve both long-range displacement and nanometer-level precision. When the position error is large, i.e., the current position is far from the target, the system should approach the target via stepping as fast as possible. Once the error falls below a critical threshold (in this paper, the threshold is 20 μm), an appropriate transition mechanism to switch from the stepping mode to the scanning mode is necessary for the system to reach the target with

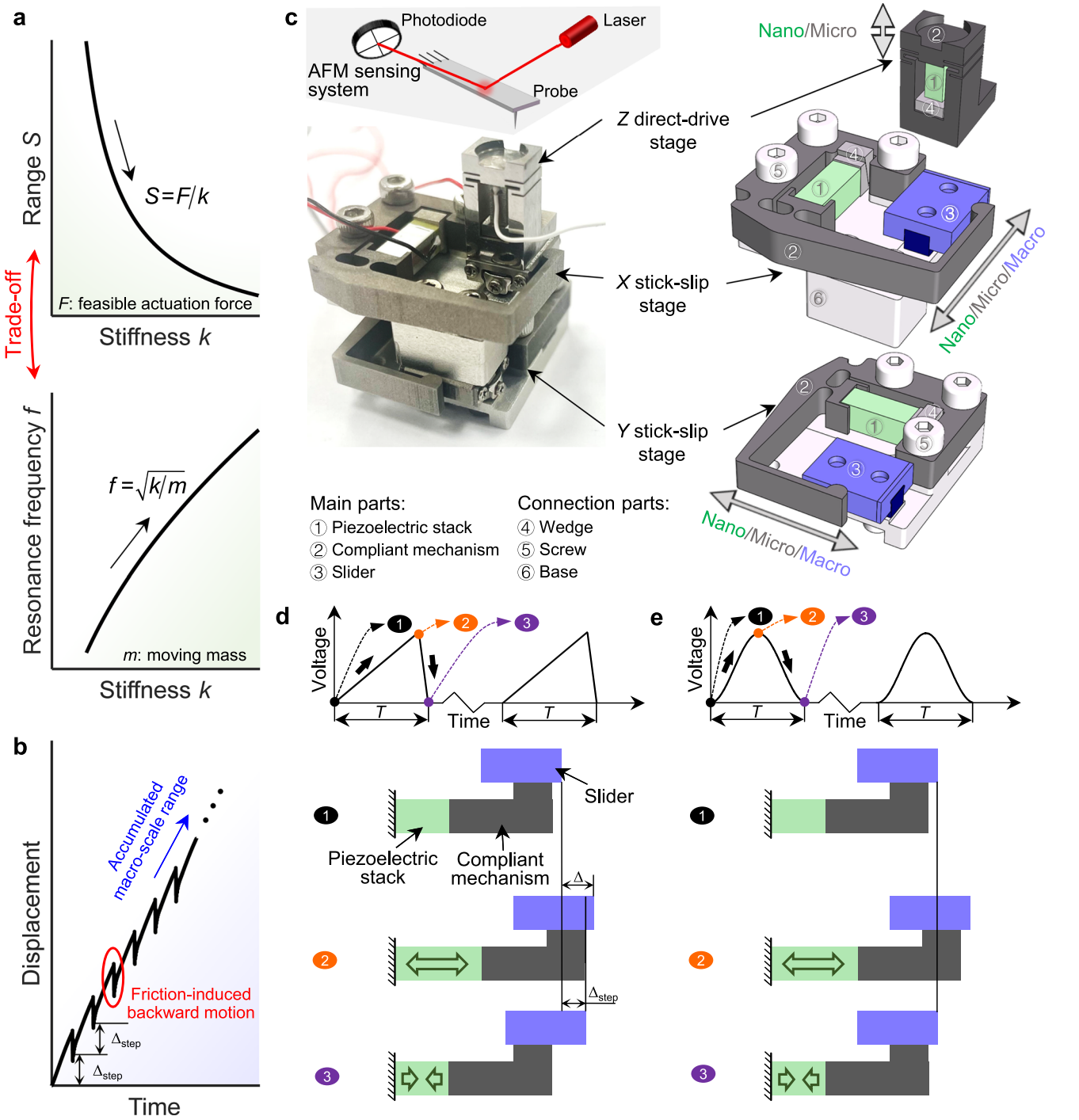

Fig. 1 | Limitations of existing nanopositioning technologies and the structure and principle of the proposed stick-slip AFM nanopositioner. a Direct-drive nanopositioners suffer from the trade-off between range and resonance frequency. **b** Stick-slip nanopositioners in pure stepping mode cannot achieve nanometer precision due to the high uncertainty caused by the friction-induced backward motion effect. **c** Structure of the proposed AFM nanopositioner. Principle of stick-slip nanopositioners in **d** the stepping mode and **e** the scanning mode. AFM: atomic force microscopy, *T*: period of the sawtooth signal, Δ: displacement at moment-2, Δ_{step}: the net step size.

nanometer precision. Control phases-1 and 2 were designed to fulfill these requirements.

In Phase-1, the stick-slip nanopositioner is excited by the optimal sawtooth signal to perform long-range stepping at the highest velocity. Therefore, the effects of the excitation parameters were explored first. We fixed the excitation frequency at 10 Hz and varied the voltage amplitude to examine its effect on stepping velocity. As shown in Fig. 2a, b, for both the *X*- and *Y*- stages, the stepping velocity increased monotonically with the voltage amplitude (also see Supplementary Fig. 4). At the maximum amplitude of 120 V, forward and reverse stepping velocities reached 121.6 μm/s and -123.2 μm/s for the *X*-stage, and 211.0 μm/s and -237.4 μm/s for the *Y*-stage. The stepping velocity of the *Y*-stage was observed to be higher than that of the *X*-stage because the backward motion effect that occurred at the end of each excitation cycle is more obvious for the *X*-stage[27,31] (Supplementary Fig. 4). Next, we selected 120 V as the optimum amplitude, and altered the excitation

https://doi.org/10.1038/s41467-025-65579-1

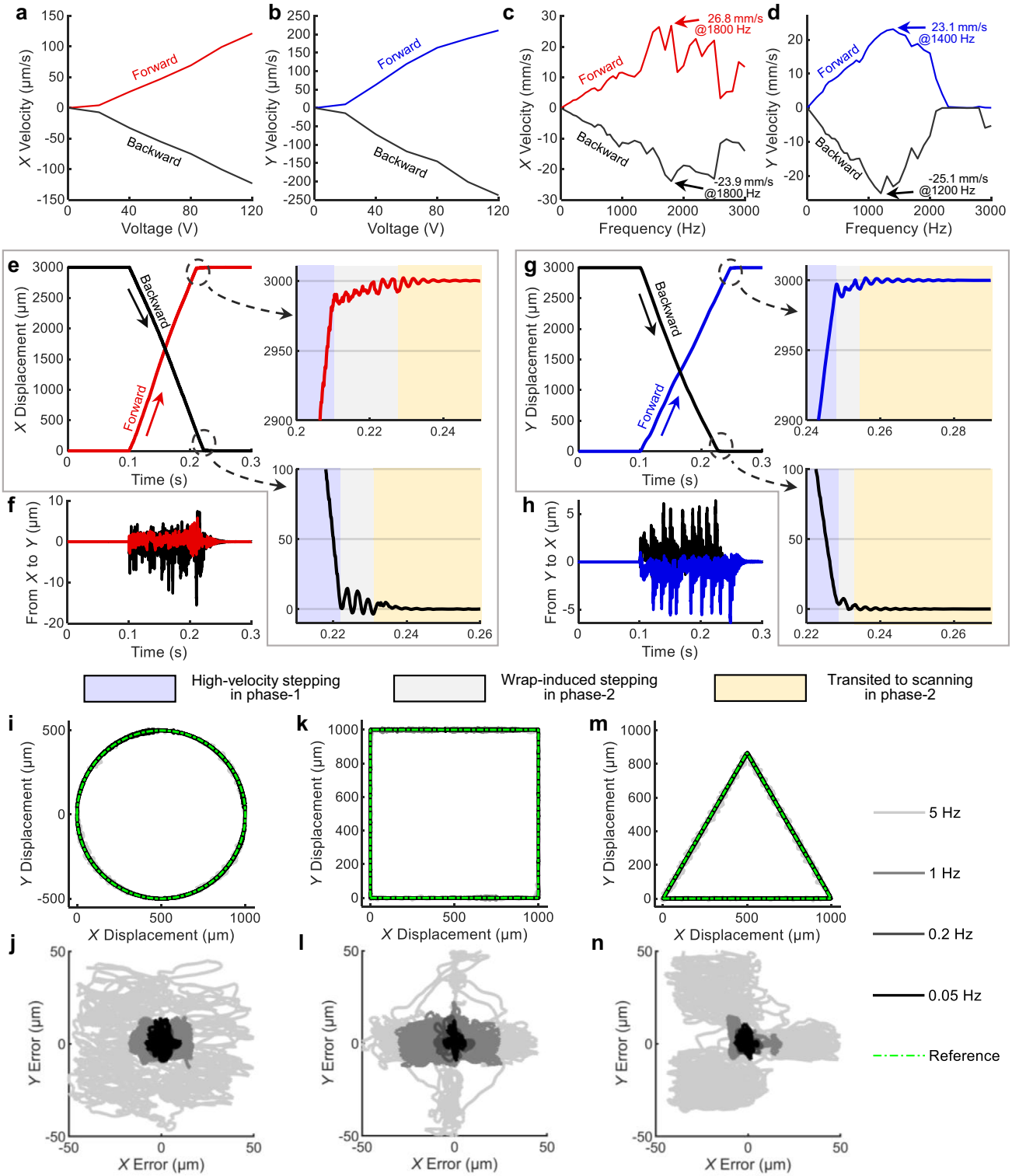

Fig. 2 | Seamless transition between stepping and scanning enables cross-scale nanopositioning and tracking. Statistical stepping velocity of the **a** *X*-stage and **b** *Y*-stage under various voltage amplitudes, and that of the **c** *X*-stage and **d** *Y*-stage under various excitation frequencies. Cross-scale point-to-point nanopositioning performance under closed-loop control. **e** Main motion and **f** parasitic motion of the *X*-axis. **g** Main motion and **h** parasitic motion of the *Y*-axis. Tracking results of the 1 mm × 1 mm **i** circular, **k** square, and **m** triangular trajectories under the frequencies of 0.05 Hz, 0.2 Hz, 1 Hz, and 5 Hz. Corresponding errors of the tracking of **j** circular, **l** square, and **n** triangular trajectories.

frequency to examine its impact on stepping velocity. From the statistical velocity curves in Fig. 2c, d (also see Supplementary Fig. 4 for displacement curves), the maximum stepping velocities along the *X*+, *X*-, *Y*+, *Y*- directions were identified as 26.8 mm/s, −23.9 mm/s, 23.1 mm/s, and −25.1 mm/s, corresponding to optimum exciting frequencies of 1800 Hz, 1800 Hz, 1400 Hz, 1200 Hz, respectively. Also, it was found that the cross-coupling effect between the axes was very small, which was less than 1% (Supplementary Fig. 5). Therefore, sawtooth signals with 120 V amplitude and these frequencies were utilized to excite the piezoelectric stacks of the nanopositioner in phase-1.

Once the macro-scale position error is reduced to below the threshold by phase-1, switching from stepping to scanning to seek a fine precision is the next problem. A widely implemented method is to control the stick-slip nanopositioner as a direct-drive one and employ an integral feedback controller (or similar)[21,22]. The integral feedback controller can be expressed as

$$C(t) = \int k_i e(t) \mathrm{d}t \tag{1}$$

where $e(t)$ denotes the position error, k_i denotes the integral gain, $C(t)$ is the state of the integral controller. However, it should be noted that the real-time generated $C(t)$ can easily exceed the maximum feasible input voltage of the piezoelectric stack (or be a negative value, which is also not feasible). The required control voltage is usually not applicable, leading to a failed control. Furthermore, under this control, the system is very difficult to track large trajectories that exceed the nanopositioner's pure scanning range. Here, in phase-2, instead of standard integral controllers, we introduce a wrap-state integral controller to govern the transition between stepping and scanning. Its output voltage signal to excite the piezoelectric stack has the expression of

$$V = \begin{cases} C & C \in [C_L, C_U) \\ C - (C_U - C_L)\left\lfloor \frac{C - C_L}{C_U - C_L} \right\rfloor & \text{otherwise} \end{cases} \tag{2}$$

where C_U= 40 V and C_L= 0 V denote the upper and lower values of the wrapped state, respectively (see Methods for detailed parameter determination). Conceptually, the wrap-state integral controller discretizes the otherwise unfeasible real-time control voltage into implementable voltage signals bounded by C_U and C_L. When C reaches C_U, the output voltage V would be reset to C_L (or to C_U when it reaches C_L). This will cause an instantaneous voltage shift, akin to the sudden drops in sawtooth signals, prompting the nanopositioner to step toward the target position (wrap-induced stepping, see Supplementary Fig. 6). After several wrap-induced steps, as the error is sufficiently small, C no longer reaches the upper or lower boundaries. In this situation, the wrapping behavior ceases and the output transitions to a continuous form, and the system seamlessly enters the scanning mode —free from kinetic friction (see Supplementary Fig. 6). Notably, during the wrap-induced-stepping process, backward motion effects also occur between successive steps. However, the associated uncertainties are compensated in the final scanning process, ensuring nanometer-level positioning precision.

The combination of control phases-1 and 2 enables a series of cross-scale nanopositioning tasks. A typical example is point-to-point motion. We sent commands to move from the 0 mm position to the 3 mm position, or vice versa, at 0.1 s, to one of the stick-slip axes. The displacements of the main motions and parasitic motions of the stages were recorded simultaneously. The main motion curves (Fig. 2e and g) reveal that both X and Y axes successfully reached the target macro position in less than 0.2 seconds, with the root-mean-square steady-state positioning errors of approximately 3.2 nm, demonstrating a nanometer-level repeatability. The major error source was the noise of the displacement sensor. The transition between the two phases, as well as the transition between wrap-induced stepping and scanning in phase-2, can be identified from the control voltage curves (Supplementary Fig. 7), and were also highlighted in the enlarged views of the main motions (Fig. 2e and g). Cross-coupling-induced parasitic motions (Fig. 2f and h) were treated as disturbances and were successfully constrained to a few microns during the stepping of the main motions. Following the transition of the main motions from stepping to scanning, the errors induced by parasitic motions ultimately reached the nanometer-level. These results demonstrate the system's ability to rapidly reduce macro-scale positioning errors to the nanometer level.

Beyond point-to-point positioning, the controller also enables cross-scale real-time tracking of arbitrary trajectories. Traditionally, the stepping velocity of stick-slip systems was controlled by changing the amplitude or frequency of the sawtooth excitation voltage[19], which lacks responsiveness to real-time changes. In contrast, the control voltage of the wrap-state integral controller (in phase-2) is dynamically generated according to the real-time position error, enabling highly flexible stepping velocity dynamically and ensuring a nanometer-level precision when the tracking ends. To demonstrate this capability, we conducted experiments of circular, square, and triangular trajectory tracking (range: 1 mm; frequency: 0.05–5 Hz; Supplementary Videos 1 to 3). In the 2-dimensional XY space, the measured trajectory curves closely matched the reference curves (Fig. 2i, k, and m), demonstrating the excellent long-range tracking capability of the stick-slip nanopositioner. Under all frequencies, the maximum and root-mean-square tracking errors for these trajectories were less than 6.2% and 3.4% of the trajectory length, respectively (see Fig. 2j, l, and n, Methods, and Supplementary Table 1). In particular, under 0.05 Hz, the maximum and root-mean-square tracking errors for all trajectories were observed to be no more than 1.4% and 0.16%, respectively. Taking the tracking of 0.05 and 5 Hz circular trajectories as examples, the time-domain displacement, position error, and voltage curves were plotted in Supplementary Fig. 8. In particular, both the X- and Y- trajectories tracked their trajectories well (Supplementary Fig. 8a, d, g, and j). At 0.05 Hz, the position error was below 20 μm for both axes throughout the tracking (Supplementary Fig. 8b and e). Therefore, the system was controlled in phase-2 alone, the voltage was bounded between 0-40 V, and the stepping was wrap-induced stepping. While at high frequencies, the time delay (Supplementary Fig. 8g and j), which is an intrinsic characteristic of all feedback controllers[8], had an increased impact on tracking errors. Therefore, the positioning errors at 5 Hz seemed like sinusoidal curves and the amplitude exceeded 20 μm (Supplementary Fig. 8h and k). Once the error exceeds 20 μm, the system switches to phase-1 (excited by 120 V sawtooth signals under the optimal frequency) automatically for rapid correction. The combination of high-velocity stepping (in phase-1) and wrap-induced stepping (in phase-2) enabled the system to effectively track this trajectory with both high frequency and long range. It is also important that, micron-level deviations only occurred during stepping. Once the trajectory ended and no more stepping was required, the system finally transited to the scanning mode and held the position with nanometer-level accuracy (Supplementary Fig. 8b, e, h and k).

Damping-tracking control enables high-bandwidth scanning

Traditionally, stick-slip nanopositioners were only used for coarse positioning and quasi-static fine positioning (such as point-to-point tasks), while dynamic scanning operations—such as high-bandwidth scanning—have relied on direct-drive systems. In this section, we investigate the dynamic behavior of stick-slip nanopositioners operating in scanning mode and demonstrate that, when combined with a damping-tracking control scheme (in control phase-3), these systems can also support high-bandwidth scanning.

We first characterized the open-loop performance of the stick-slip stages in the scanning mode, focusing on their range and frequency response. A 1-Hz sinusoidal signal with an amplitude of 120 V was applied to the piezoelectric stacks, resulting in the output main motions of 21.3 μm and 24.3 μm in the X- and Y- axes, respectively (Fig. 3a). These values represent the maximum scanning ranges achievable without stepping, and thus define the maximum area of a single AFM frame. The slight differences between the pure scanning ranges of the two axes might be due to the inherent performance differences between the piezoelectric stacks and the difference between preloading forces. Cross-coupling effects were very small

https://doi.org/10.1038/s41467-025-65579-1

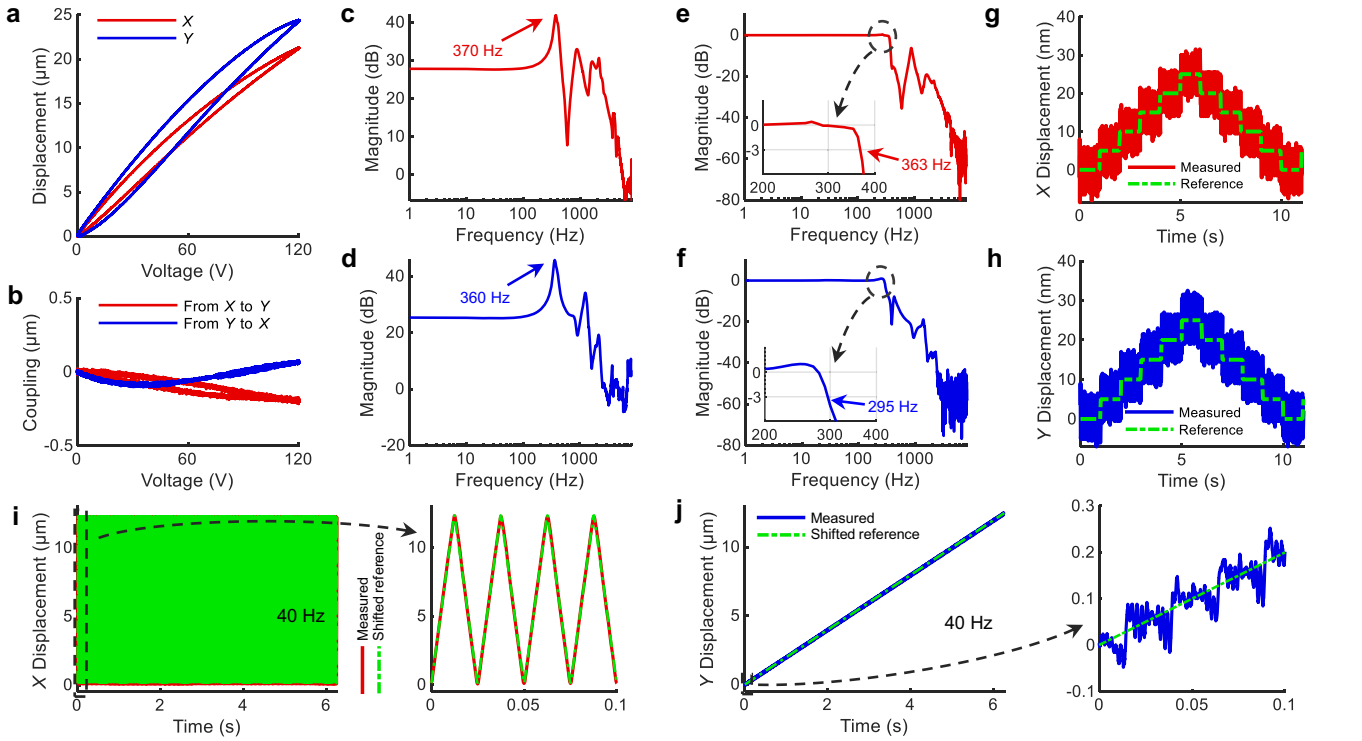

Fig. 3 | Damping-tracking control enables high-bandwidth scanning. Open-loop scanning performances. Input-output relationship of the **a** main motion and **b** parasitic motion under the 1 Hz *X*- and *Y*-axial sinusoidal voltage excitation. Amplitude-frequency responses of **c** the *X*-stage and **d** the *Y*-stage. **e**–**j** High-bandwidth scanning performances in control phase-3. Closed-loop amplitude-frequency responses of **e** the *X*-stage and **f** the *Y*-stage. 5 nm stair signals scanning results of **g** the *X*-stage and **h** the *Y*-stage. **i** *X*-axial and **j** *Y*-axial displacement curves of the raster scanning under 40 Hz.

(Supplementary Text), with parasitic motions of 0.2 μm from *X* to *Y* and 0.13 μm from *Y* to *X* (Fig. 3b), both under 1% of the main motions. To investigate the frequency responses, chirp voltages with frequency ranging from 0.1 to 10000 Hz were fed to the piezoelectric stacks. The amplitude of the voltages was sufficiently small (2 V) to avoid inducing kinetic friction. By employing the Fourier transformation of the voltage signal and the measured displacement, sharp dominant resonance peaks at 370 Hz and 360 Hz were found in the amplitude-frequency responses of the *X*- and *Y*- stages, respectively (Fig. 3c and d). The difference in resonance frequencies between the *X*- and *Y*- axes primarily results from the difference in moving mass. Factors such as machining tolerances, variations between the two piezoelectric stacks, and preload forces also affect the resonance frequency.

These results suggest that in scanning mode, the stick-slip nanopositioner exhibits several typical control challenges, including hysteresis nonlinearities (Fig. 3a), cross-coupling, and lightly-damped resonances—similar to those found in direct-drive systems. To solve these issues, we employed a notch filter as the damping controller to suppress the sharp resonance peaks, thereby increasing the gain margin (see in Methods for parameter determination). Then, a high-gain proportional-integral controller was employed as the tracking controller (see Methods), treating the effects of hysteresis and cross-coupling as disturbances to be rejected.

Under this damping-tracking control scheme, the closed-loop frequency responses (Fig. 3e and f) revealed -3 dB control bandwidths of 363 Hz and 295 Hz for the *X*- and *Y*- stages, respectively, both of which are dozens of times higher than those of conventional millimeter-range nanopositioners driven by voice coil motors[32,33]. Then, 5 nm staircase reference signals were scanned by the nanopositioner to demonstrate the resolution. The measured displacement data (Fig. 3g and h) clearly resolved individual steps, confirming that both the *X*- and *Y*-axes had a nanometer-level fine resolution. It should be noted that, the resolution of the system was basically limited by the resolution and noise of the displacement sensor. When the resolution of the sensor can be improved (at a cost of a smaller measurement range) and/or the data can be smoothed (at a cost of a lower response speed), the positioning resolution can be refined to the sub-nanometer level (see in Methods and Supplementary Fig. 9)[34]. Next, raster scanning tests were performed over a 12.5 μm × 12.5 μm area. The *X*-axis acted as the fast axis and scanned the periodical triangular trajectories, while the *Y*-axis acted as the slow axis and scanned a ramp signal. The number of scanning periods was 250. Considering the control bandwidth of the system, the highest scanning rate for the *X*-axial triangular signal was set as 40 Hz. Once the impact of the time delay had been eliminated by data post-processing, the root-mean-square errors (see Methods and Supplementary Table 2) for each axis were found to be only 0.044% and 0.023% of the 12.5 μm working range at 1 Hz. As the frequency increased, the error also grew (Supplementary Table 2). Figure 3i and j illustrate the displacements recorded at a scanning line rate of 40 Hz. At 40 Hz, the root-mean-square scanning error for the *X*-axis remained below 1.27%, while that for the *Y*-axis was only 0.386%. Given the high scanning rate, these minor errors are deemed acceptable for most application scenarios. These results can ensure a minimal *XY* distortion in the following AFM imaging experiments.

Cross-scale high-bandwidth AFM imaging

The above experiments demonstrate the excellent nanopositioning performance from the nano to the macro scale, laying a solid foundation for the construction of cross-scale high-bandwidth application systems. In particular, the high resolution and repeatability ensure the quality of the data, the high-bandwidth scanning ability supports a high line rate during the AFM raster scanning, while the cross-scale positioning and tracking functionality enables rapid and precise switching between multiple areas of interest. As a comprehensive demonstration, this section investigates the application of the

https://doi.org/10.1038/s41467-025-65579-1

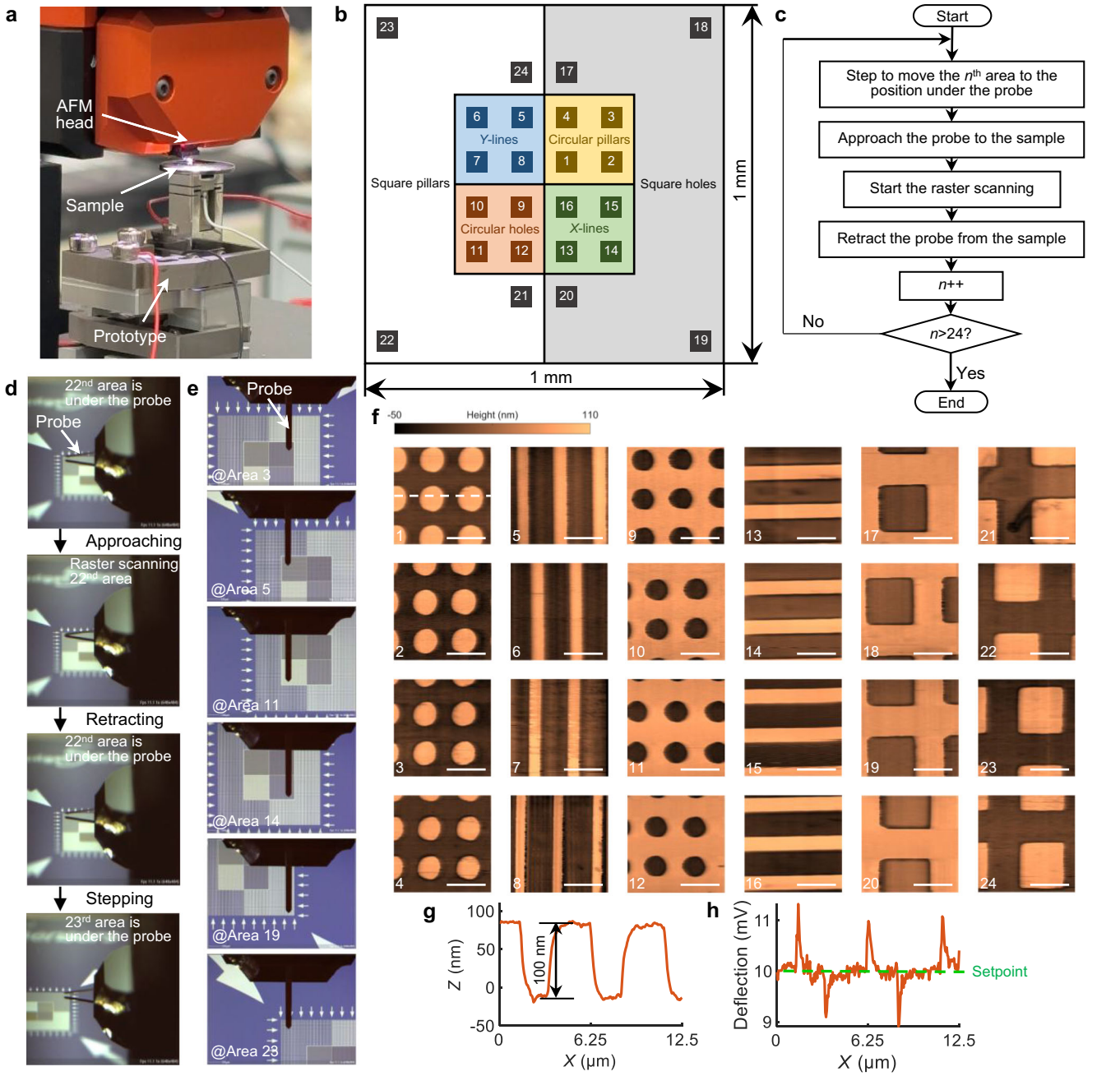

Fig. 4 | Cross-scale high-bandwidth AFM sampling imaging. a Photograph of the integrated system. **b** Schematic diagram of areas of interest on a 1 mm × 1 mm height calibration standard. **c** Block diagram of the imaging process. **d** Side views for illustrating the imaging processes. **e** Top views for presenting the relative positions between the probe and the sample. **f** AFM images of the 24 areas, scale bar: 5 μm, scanning rate: 40 Hz, resolution: 250 × 250 pixels. **g** Profile and **h** deflection signal corresponding to the cross-section line marked in the 1st area of **f**.

proposed stick-slip nanopositioning system, equipped with the triple-phase controller, in cross-scale high-bandwidth AFM imaging.

An integrated AFM system was constructed (Fig. 4a), in which the stick-slip nanopositioner carried the sample to achieve three degrees of freedom motion. Meanwhile, the probe-sample interaction was monitored via the deflection signal from a commercial AFM head, which served as the feedback signal for constant-force control of the *Z*-stage (see in Methods and Supplementary Fig. 10). The approaching and retracting processes for the probe were performed by a vertical motor in the AFM head.

A cross-scale high-bandwidth AFM sampling imaging experiment was carried out on a commercial height calibration standard (Supplementary Video 4). As illustrated in the schematic (Fig. 4b), the sample featured six typical structure arrays. Among them, the square holes and pillars with a 10 μm pitch were arranged in a 1 mm × 1 mm square; the circular pillars and holes, and the *X*- and *Y*- lines with a 5 μm pitch were arranged in a 500 μm × 500 μm square. The integrated AFM system was programmed to automatically image four areas on each array, yielding a total of 24 images (with the sequence labeled in Fig. 4b). Each image was acquired through a 250 × 250-pixel scan over a 12.5 μm × 12.5 μm area, yielding a planar resolution of 50 nm. The scanning rate was set as 40 Hz. Supplementary Table 3 summarizes the coordinates of the starting points for each scan. To prevent the significant variation of the tip-sample interaction force during the

stepping process (Supplementary Fig. 11), which may be due to the cross-coupling from *XY* to *Z* and the potential sample tilt (which may exceed the *Z*-axial range and damage the tip or sample), the approaching and retracting processes were inserted between the acquisition of successive AFM images, ensuring stepping occurred only out of contact (Fig. 4c). At the beginning of the experiment, the nanopositioner stepped to move the 1st area to the position under the probe. Then, the system approached the probe to the sample. Thereafter, the *XY* raster scanning commenced, while the *Z*-stage tracked the surface topography. Once the scanning of this area was complete, the AFM head retracted the probe from the sample, and the system prepared for the scanning of the next area. By repeating these steps, the system can automatically complete the AFM experiment with 24 images (Fig. 4c). The approaching, retracting, and stepping processes can be observed in the photos in Fig. 4d. Figure 4e depicts the top views of the system when imaging one area of each of the six arrays, showing the relative planar positions between the probe and the sample. The imaging results of the 24 areas illustrate the imaging quality of this system (Fig. 4f), demonstrating that clear and high-resolution images can be successfully captured at any position within a millimeter-level area. To better evaluate the imaging quality, Fig. 4g depicts a cross-section of the line marked in the 1st area of Fig. 4f, wherein the circular pillars' height (100 nm) can be clearly identified. The deflection signal (Fig. 4g) varied only around the edges of the pillars, while it was mostly constant (at the setpoint of 10 mV) on the flat area, indicating that the *Z*-stage tracked the surface topography well, demonstrating a satisfactory imaging quality[35]. The complete AFM imaging process, including approaching, scanning, retracting, and stepping, was finished in 12 min 19 s (Supplementary Fig. 12 and Supplementary Video 4), demonstrating a substantial increase in throughput while maintaining a high imaging quality. It should be noted that, for the most common conventional cross-scale AFM sampling measurement method (typically has a scanning rate of less than 5 Hz, and moves the sample from one position to another using a manual or motorized coarse stage)[36], they may take 1 h to image less than ten 250 × 250-pixel AFM images. Therefore, this approach achieves a 1–2 order of magnitude efficiency improvement over conventional methods.

The sampling imaging experiments demonstrated the system's capability to acquire multiple micron-scale images across a millimeter-scale range with high efficiency. In fact, such sampling already satisfies the demands of most applications. Nevertheless, certain scenarios may require larger-area images. The following experiments show that the proposed stick-slip system can support the acquisition of millimeter-scale large AFM images via stitching. Figure 5a shows the schematics of stitching, the overall image was generated by stitching several individual AFM frames, each covering an area of 12.5 µm × 12.5 µm with a resolution of 100 × 100 pixels. To facilitate stitching, adjacent frames were spaced 10 µm apart in the *X*- or *Y*- direction, ensuring a 20% overlap. The overall image acquisition procedure was similar to that used in the above AFM sampling imaging experiments (Fig. 4c), with the only difference being the positions of the areas of interest. The scan line rate was set to be 20 Hz. The AFM stitching imaging was carried out on the commercial height calibration standard first. A linear array of 100 × 1 frames was acquired in series (Fig. 5b and Supplementary Fig. 13), and a composite image covering 1025 µm × 12.5 µm was obtained using commercial stitching software (Fig. 5c, also see in Supplementary Data 1 for a full-size image). As shown in Fig. 5c, the stitched image clearly reflects the surface morphology with very small distortion. The same procedure was then applied to a microchip sample featuring 350 nm-high structures with an approximate pitch of 900 nm. A total of 10 × 10 AFM frames were acquired (Fig. 5d and Supplementary Fig. 14), and stitched into a large image covering 102.5 µm × 102.5 µm (Fig. 5e). The feature structures, scratches, and stains were clearly visible, demonstrating the high image quality.

Discussion

Advancing the range and bandwidth of nanopositioning is the most straightforward and fundamental way to enhance the performance of AFM and many other precision instruments. Collectively, the work shown here is the start of a family of AFM nanopositioning technology with a millimeter-level motion range, a nanometer-level precision, and a hundreds-of-Hertz-level high bandwidth. Although existing nanopositioning systems feature one or two of these characteristics, the proposed triple-phase-controlled stick-slip system embraces all three properties. The synthesis of these superiorities has enabled a series of advanced nanopositioning tasks, including high-speed cross-scale nanopositioning and tracking, and high-bandwidth AFM scanning. These implementations of the proposed method could be used to understand both its effectiveness and potential for improving and extending towards broader applications in the future.

To illustrate the system's advantages in nanopositioning, Table 1 compares its performance against representative direct-drive and stick-slip piezoelectric nanopositioners from leading manufacturers, including Physik Instrumente[37], SmarAct[38], Attocube[39], and Thorlabs[40].

In the scanning performance, it is noteworthy that key dynamic metrics, such as resonance frequency and control bandwidth, were rarely reported for commercial stick-slip systems. Even among direct-drive systems, only Physik Instrumente provides such specifications. Yet, these parameters are critical in determining operational speed and imaging quality. Our system demonstrated a competitive resonance frequency and achieved a control bandwidth approaching this frequency in phase-3, higher than all systems listed in Table 1. Direct-drive systems are commonly used for conducting the scanning motion. Thus, they all have at least dozens of microns scanning range. Due to the elaborately designed compliant mechanism with flexure amplification structure, P-629.2CD by Physik Instrumente reached performances comparable to voice-coil actuated systems[12,13]. It provides an 1800 µm large scanning range, but at a cost of a low frequency (only 60 Hz). In contrast, stick-slip systems have traditionally used scanning mode only for compensating stepping errors. Consequently, they paid very little attention to the scanning mode motion ranges—less than 3.5 µm—which was even smaller than the pitch size of standard height calibration gratings (generally 5 µm) and insufficient for most AFM applications. Our system, however, provided a pure scanning range exceeding 21.3 µm, nearly an order of magnitude greater than the compared stick-slip products. By further combining scanning and stepping motions, stitching methods can be employed to enable millimeter-scale AFM imaging. As for the stepping performances, our system exhibited the highest stepping velocity in all directions (*X*+, *X*-, *Y*+, *Y*-). To keep the overall system compact, we adopted relatively small sliders as end-effectors, which limits the stepping range. However, if needed, the range can be readily extended by using longer sliders. In point-to-point positioning tests, the system demonstrated 3.2 nm repeatability over its full 3 mm motion range—1-2 orders of magnitude better than commercial stick-slip devices, and comparable to direct-drive systems with only 60 µm range. In summary, our system integrates the respective advantages of both direct-drive and stick-slip nanopositioners in terms of range, dynamic performance (resonance frequency and bandwidth), and repeatability (Fig. 6a).

In order to assess various characteristics of the proposed stick-slip AFM system comprehensively, we compared its operation range, bandwidth, structural compactness, and system simplicity with other AFM technologies, including piezoelectric-actuated[41], normal-stressed electromagnetic-actuated[15], and voice coil-actuated[13] direct-drive nanopositioners, multi-stage positioning systems[20], as well as multi-probe AFM systems[42] (Fig. 6b).

It can be found that, among single-stage systems, our approach is unique in achieving both millimeter-level long range and hundreds-of-Hertz-level high bandwidth. In contrast, all direct-drive nanopositioners suffer from the trade-off between the range and the bandwidth.

https://doi.org/10.1038/s41467-025-65579-1

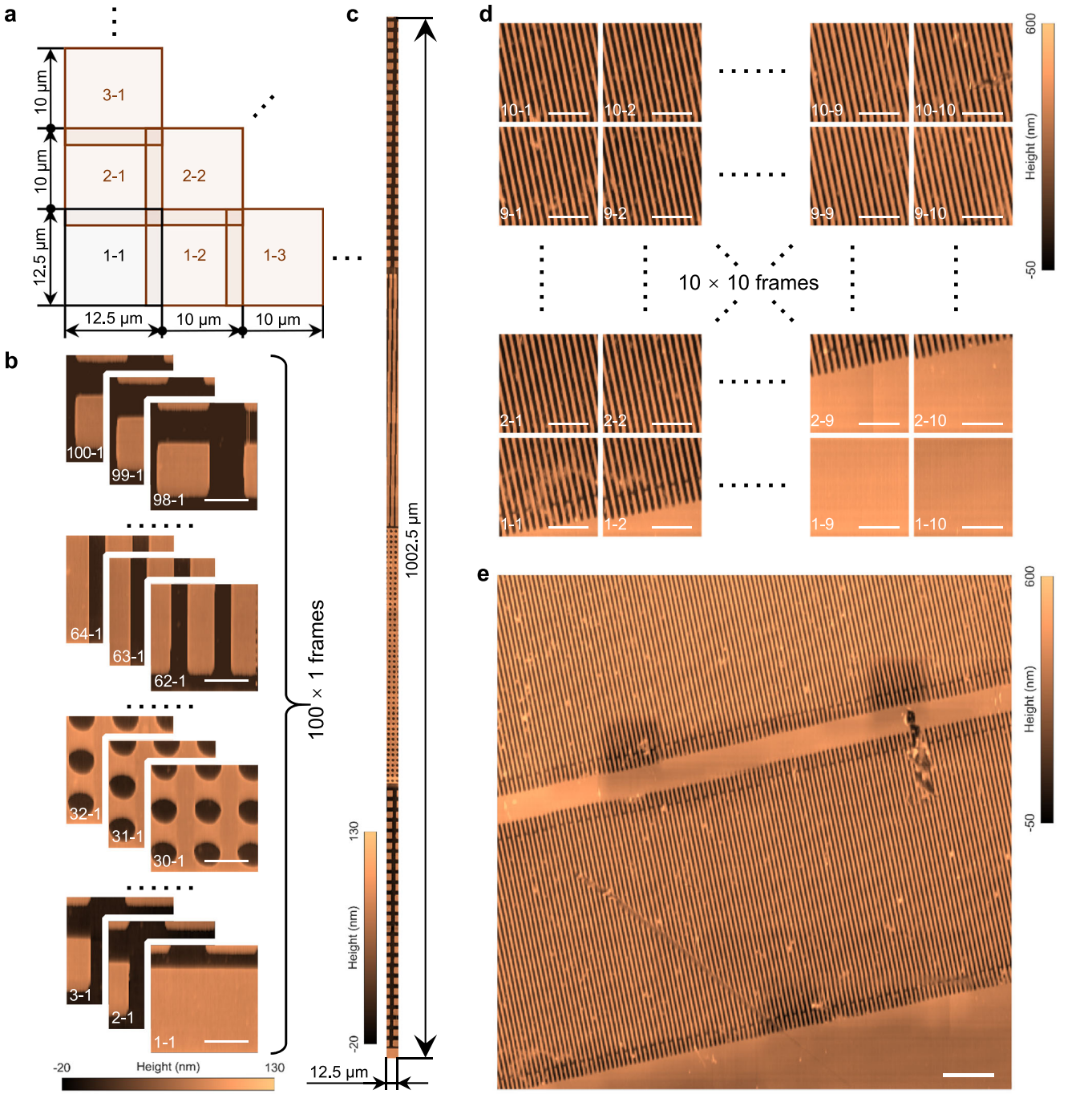

Fig. 5 | Cross-scale high-bandwidth AFM stitching imaging. a Schematic of the stitching process, illustrating 20% overlap and relative positions of adjacent AFM image frames. **b** A sequence of 100 × 1 AFM frames acquired on a height calibration standard, scale bar: 5 µm, scanning rate: 20 Hz, resolution: 100 × 100 pixels per frame. **c** Millimeter-scale composite image stitched from the 100 × 1 frames, final resolution: 8020 × 100 pixels. **d** A grid of 10 × 10 AFM frames collected on a chip sample, scale bar: 5 µm, scanning rate: 20 Hz, resolution: 100 × 100 pixels per frame. **e** Composite image stitched from the 10 × 10 frames, final resolution: 820 × 820 pixels, scale bar: 10 µm.

Moreover, the dimension of direct-drive systems is typically correlated with the achievable range. For example, the lateral dimension of a millimeter-range voice coil-actuated nanopositioner is typically several decimeters, while the proposed system only requires 26 mm, comparable to a piezoelectric-actuated direct-drive nanopositioner. In terms of system simplicity, piezo- and voice coil-based direct-drive nanopositioners are the simplest. The proposed stick-slip system, which essentially adds a slider to a piezoelectric direct-drive stage, achieves high simplicity with enhanced functionality. Normal-stressed electromagnetic-actuated systems, however, are more complex, as they lack commercially available actuators, requiring researchers to custom-fabricate these components. A multi-stage architecture—combining long-range stages for coarse motion (such as stepping motors or stick-slip nanopositioners in pure stepping mode) and short-range stages (such as piezoelectric direct-drive stages) for fine motion—can be developed for achieving both long range and high bandwidth[20], and have been adopted in many commercial AFM products. However, such systems require multiple actuators and sensors per axis, significantly increasing complexity, size, and cost. They also suffer from dynamic coupling effects that introduce vibrations and

https://doi.org/10.1038/s41467-025-65579-1

Table 1 | Performance comparison with representative direct-drive and stick-slip piezoelectric nanopositioners

Manufacturer	Model	Principle	Performance					
			Resonance frequency	Control bandwidth	Pure scanning range	Stepping range	Stepping velocity	Repeatability
This work	**This work**	**Stick-slip**	**>360 Hz**	**>295 Hz**	**>21.3 μm**	**>3 mm**	**>23.1 mm/s**	**3.2 nm**
Physik Instrumente	P-620.2CD	Direct-drive	575 Hz	267 Hz	60 μm	/	/	2 nm
	P-629.2CD	Direct-drive	60 Hz	33 Hz	1800 μm	/	/	14 nm
	Q-521.340	Stick-slip	/	/	/	32 mm	6 mm/s	/
	Q-545.240	Stick-slip	/	/	/	26 mm	8 mm/s	/
SmarAct	PLF3232-xy.60	Direct-drive	/	/	60 μm	/	/	/
	SLC-2445	Stick-slip	/	/	1.3 μm	29 mm	20 mm/s	40 nm
	SLC-2445-F	Stick-slip	/	/	1 μm	29 mm	20 mm/s	25 nm
Attocube	ANSxy50/RT	Direct-drive	/	/	30 μm	/	/	/
	ANPx51/RT	Stick-slip	/	/	3.5 μm	3 mm	1 mm/s	/
	ECSx3030/AI/RT	Stick-slip	/	/	1.6 μm	20 mm	4.5 mm/s	/
Thorlabs	PDX1	Stick-slip	/	/	/	20 mm	20 mm/s	750 nm
	PDX2	Stick-slip	/	/	/	5 mm	8 mm/s	500 nm

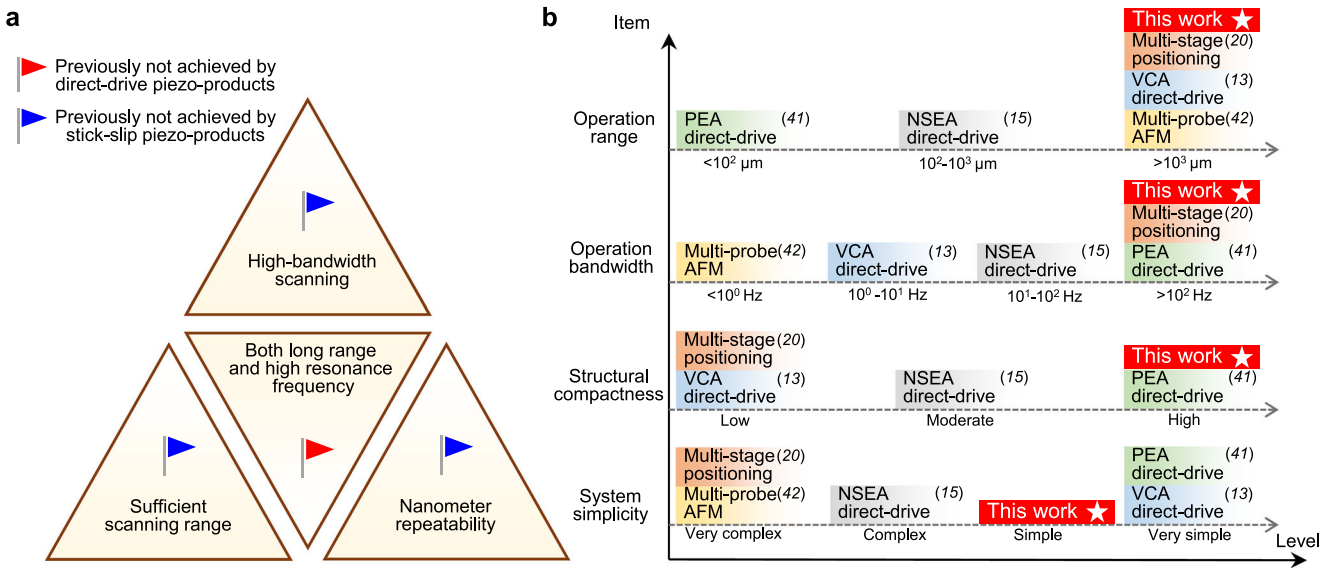

Fig. 6 | Summary and comparison of the proposed stick-slip system. a The proposed system achieved four advanced nanopositioning characteristics that are not simultaneously attainable with existing direct-drive or stick-slip products. **b** Comparison of the proposed stick-slip AFM system with representative AFM technologies. PEA piezoelectric actuated, VCA voice coil actuated, NSEA normal-stressed electromagnetic actuated.

control difficulties[43]. By contrast, the proposed system met these requirements by introducing a triple-phase controller to enhance the performance of a typical single-stage (one actuator and one sensor per axis) stick-slip nanopositioner, and thus offers a compelling alternative to complex, bulky, and expensive multi-stage systems. Multi-probe AFM parallel imaging is a totally different strategy for improving imaging throughput, its AFM head employs arrays of probes to scan large areas simultaneously. However, such systems are costly and systematically complex, and currently operate at very low bandwidths (typically <1 Hz), largely due to limited nanopositioning performance. Given the demonstrated advantages of the proposed stick-slip system in a single-probe AFM setup, it is reasonable to deduce that integrating our nanopositioning system with a multi-probe AFM head could further scale up the imaging throughput. In short, compared to existing AFM technologies, the triple-phase-controlled stick-slip AFM system combines long range, high bandwidth, compact size, and high simplicity within a single-stage, single-probe architecture.

The triple-phase controller is the key to enabling a typical stick-slip stage to deliver multifunctionality not previously reported. In fact, phases-1 and 3 can be viewed as targeted enhancements of stepping and scanning performance, respectively. In applications where neither high-stepping velocity nor wide control bandwidth is critical, the controller can be simplified to a wrap-state integral controller (i.e., phase-2 only), omitting phases-1 and 3, which would still satisfy the cross-scale function demands of most scenarios. It should be noted that, the proposed controller was designed for error suppression and is thus well suited for tracking or scanning arbitrary trajectories. When the trajectories are predefined, learning-based control algorithms such as repetitive control[44] and iterative learning control[45] can be further adopted to enhance the scanning accuracy and frequency.

From a design perspective, the current prototype was developed to meet the growing performance demands of AFM imaging. Therefore, it includes two stick-slip axes and one direct-drive axis. For applications that need tri-axial cross-scale high-

bandwidth motion, the *Z*-axis could also be designed by using stick-slip principle. In fact, stick-slip piezoelectric systems can realize not only linear motions, but also rotational motions[17,28]. Given their ability to provide long-range, high-frequency, and high-precision motion, future devices based on the stick-slip principle hold promise for improving throughput in many cutting-edge scenarios, such as robotic surgery[46], micro assembly[47], biological puncture[48], and scanning probe lithography[49].

Methods

Prototype design and fabrication

The computer-aided-design model for the proposed nanopositioner was established using Solidworks 2021 (Fig. 1c). By introducing the material properties into the computer-aided-design model, finite element simulations were carried out using ANSYS Workbench 2021. The piezoelectric stacks (PSt3.5×3.5/7 for the *X*- and *Y*- stages, PSt2×3/5 for the *Z*-stage, Piezomechanik, Germany), sliders (BWU8-10, IKO, Japan), and screws were commercially available. The compliant mechanisms of the *X*- and *Y*- stages were made of TC4 titanium alloy, and that of the *Z*-stage was made of stainless steel S136. They were fabricated by wire electrical discharge machining tool. Other parts were fabricated with 7075 aluminum alloy by computer numerical control machining tool. Structural parameters of the compliant mechanisms are illustrated in Supplementary Figs. 1 and 2.

Experimental setup

The control algorithms were written in MATLAB/Simulink 2023b, which were downloaded to the dSPACE board (MicroLabBox, dSPACE GmbH, Germany). The 16-bit digital-to-analog converters of the dSPACE board output the analog voltage signals, which were supplied to two voltage amplifiers (E01.A2, CoreMorrow, China, amplification ratio: 20, for the *X*- and *Y*- stages; HVA200, THORLABS, USA, amplification ratio: 20, for the *Z*-stage) to generate the excitation voltages for the piezoelectric stacks. The *X*- and *Y*- axial displacements were measured by the interferometric displacement sensors (IDS3010 with probe D4/F17, Attocube, Germany) and recorded by the digital input/output module of the dSPACE. The displacement sensors allowed online adjustment of the balance between resolution and measurement range. For sub-nanometer-level positioning resolution demonstrations (Supplementary Fig. 9), we set the resolution as 0.05 nm, in such a case, the sensors provided an approximately 0.5 mm measurement range. All other experiments used 0.5 nm resolution, corresponding to a range of approximately 5 mm. The sampling frequency of the experimental setup was set to 20 kHz.

The AFM imaging experiments were carried out in constant-force contact mode. A commercial AFM head (Nanite, Nanosurf, Switzerland) equipped with a contact-mode probe (ContAl-G, BudgetSensors, Bulgaria, force constant: 0.2 N/m) was used. The deflection signal was collected by the analog-to-digital converters of the dSPACE and was used as the feedback control signal of the *Z*-stage. The height calibration standard sample (HS-100MG, BudgetSensors, Bulgaria) has a 100 nm step height. The microchip sample was provided by Shanghai Institute of Optics and Fine Mechanics, Chinese Academy of Sciences. The photographs in Fig. 4d and e were taken with the built-in cameras in the AFM head. The stitching process was conducted using the commercial software MountainsMap.

A photograph of the main experimental setup can be found in Supplementary Fig. 15. All experiments were conducted under ambient conditions, where noise may have originated from floor vibrations, air flow, and electrical interference.

Implementation and parameters of the controller

The triple-phase control algorithm was presented for controlling the *X*- and *Y*- stick-slip stages (Supplementary Fig. 3). In particular, the algorithms in control phases-2 and 3 were in a feedback manner. However, there were lightly-damped resonance peaks in the amplitude-frequency responses (Fig. 3c and d), which would cause poor gain margins. Therefore, to implement the algorithms with sufficient gains, notch filters $C_{\mathrm{NF}}(s)$ were introduced to dampen these peaks. For the *X*- and *Y*- stages, they were determined as

$$C_{\mathrm{NF},X}(s)=\frac{s^2+242.1820s+6.2900\times10^6}{s^2+2.5427\times10^3s+6.2900\times10^6} \tag{3}$$

and

$$C_{\mathrm{NF},Y}(s)=\frac{s^2+62.5328s+5.6995\times10^6}{s^2+2.3101\times10^3s+5.6995\times10^6} \tag{4}$$

respectively. From the amplitude-frequency responses of the damped systems (Supplementary Fig. 16), it can be observed that the sharp dominant resonance peaks were successfully suppressed.

In control phase-2, the value of the integral gain k_{i} of the wrap-state integral controller was selected as 20 for both the *X* and *Y* axes to ensure efficient stepping and rapid settling. C_{U}= 40 V and C_{L}= 0 V were chosen the upper and lower values of the wrapped state, respectively. Therefore, the control voltage in phase-2 is consistently maintained between 0 V and 40 V, thereby ensuring a sufficient range of at least 80 V (with the maximum input voltage being 120 V) to support the forthcoming high-bandwidth nano-precision scanning in phase-3.

High-gain proportional-integral controllers were employed in control phase-3 for a high-bandwidth control of the *X*- and *Y*- stages. The proportional-integral controller can be expressed as

$$C_{\mathrm{PI}}(s)=k_{\mathrm{p}}+\frac{k_{\mathrm{i}}}{s} \tag{5}$$

where k_{p} and k_{i} denote the proportional and integral gains of the controller, respectively. With the goal of maximizing the control bandwidth, the parameters were elaborately selected as $k_{\mathrm{p}}=0.01$, $k_{\mathrm{i}}=44$, for the *X*-stage, and $k_{\mathrm{p}}=0.01$, $k_{\mathrm{i}}=40$, for the *Y*-stage, respectively. The amplitude-frequency responses of the closed-loop systems can be found in Fig. 3e and f.

In constant-force contact mode AFM imaging, the goal of the *Z*-axial control is essentially to keep the deflection signal constant at the setpoint. In this work, the setpoint of the deflection signal was selected as 10 mV (Fig. 4h). A simple integral controller was employed for conducting the feedback control (Supplementary Fig. 10a), which has the expression of

$$C_{\mathrm{I}}(s)=\frac{k_{\mathrm{i}}}{s} \tag{6}$$

The gain was chosen as $k_{\mathrm{i}}=160000$ in order to achieve a balance between bandwidth and stability. The closed-loop amplitude-frequency response demonstrates that a *Z*-axial bandwidth of 1790 Hz was attained (Supplementary Fig. 10b).

Position error evaluation

The criteria for evaluating the position errors of tracking and scanning operations are different. The tracking tasks require the nanopositioner to follow the arbitrary position of the object in real-time. Conversely, the scanning tasks let the nanopositioner scan a predefined trajectory, it is preferable to achieve a perfectly delayed tracking rather than an imperfect timely tracking. Therefore, errors resulting from the time delay can be tolerated for the scanning tasks.

For evaluating the single-axial position error of a tracking task, the maximum error

$$e^i_{\max} = \frac{\max_{t\in(0,T]}|r_i(t) - x_i(t)|}{\max(r_i(t)) - \min(r_i(t))} \tag{7}$$

and root-mean-square tracking error

$$e^i_{\mathrm{RMS}} = \frac{\sqrt{\frac{1}{T}\sum_{t\in(0,T]}[r_i(t) - x_i(t)]^2}}{\max[r_i(t)] - \min[r_i(t)]} \tag{8}$$

were chosen as the indicators, where $i = X, Y$, $r_i(t)$ and $x_i(t)$ denote the X- or Y- axial reference trajectory and output displacement, respectively. For a two degrees of freedom tracking, the errors in the XY plane can be further calculated by

$$e_{\max} = \sqrt{{e^X_{\max}}^2 + {e^Y_{\max}}^2} \tag{9}$$

and

$$e_{\mathrm{RMS}} = \sqrt{{e^X_{\mathrm{RMS}}}^2 + {e^Y_{\mathrm{RMS}}}^2} \tag{10}$$

For evaluating the single-axial position error of a scanning task, the impact of the time delay had been eliminated[50,51], and the maximum scanning error and the root-mean-square scanning error can be expressed as

$$\hat{e}^i_{\max} = \frac{\max_{t\in(0,T]}|\hat{r}_i(t) - x_i(t)|}{\max(\hat{r}_i(t)) - \min(\hat{r}_i(t))} \tag{11}$$

and

$$\hat{e}^i_{\mathrm{RMS}} = \frac{\sqrt{\frac{1}{T}\sum_{t\in(0,T]}[\hat{r}_i(t) - x_i(t)]^2}}{\max[\hat{r}_i(t)] - \min[\hat{r}_i(t)]} \tag{12}$$

respectively. In Eqs. (11) and (12), $\hat{r}(t) = \hat{r}(t - \hat{k}T_s)$ denotes the shifted reference, where T_s is the sampling period of the experimental setup, and $\hat{k}$ denotes the number of the delayed sampling periods. The value of $\hat{k}$ is determined by solving

$$\hat{k} = \arg\min_k \left[\max_{t\in[0,T]}|r_i(t - kT_s) - x_i(t)|\right] \tag{13}$$

For a two degrees of freedom scanning, the errors in the XY plane can be expressed as

$$\hat{e}_{\max} = \sqrt{{\hat{e}^X_{\max}}^2 + {\hat{e}^Y_{\max}}^2} \tag{14}$$

and

$$\hat{e}_{\mathrm{RMS}} = \sqrt{{\hat{e}^X_{\mathrm{RMS}}}^2 + {\hat{e}^Y_{\mathrm{RMS}}}^2} \tag{15}$$

Data availability

Relevant data supporting the key findings of this study are available within the article and the Supplementary Information file. All raw data generated during the current study are available from the corresponding authors upon request.

References

1. Sellies, L. et al. Single-molecule electron spin resonance by means of atomic force microscopy. *Nature* **624**, 64–68 (2023).
2. Krieg, M. et al. Atomic force microscopy-based mechanobiology. *Nat. Rev. Phys.* **1**, 41–57 (2019).
3. Binnig, G., Quate, C. F. & Gerber, C. Atomic Force Microscope. *Phys. Rev. Lett.* **56**, 930–933 (1986).
4. Ma, R. et al. Atomic imaging of the edge structure and growth of a two-dimensional hexagonal ice. *Nature* **577**, 60–63 (2020).
5. Lansky, S. et al. A pentameric TRPV3 channel with a dilated pore. *Nature* **621**, 206–214 (2023).
6. Zhu, K. et al. Hybrid 2D–CMOS microchips for memristive applications. *Nature* **618**, 57–62 (2023).
7. Bian, K. et al. Scanning probe microscopy. *Nat. Rev. Methods Prim.* **1**, 36 (2021).
8. Huang, W.-W. et al. Design, modeling and control of high-bandwidth nano-positioning stages for ultra-precise measurement and manufacturing: a survey. *Int. J. Extrem. Manuf.* **6**, 062007 (2024).
9. Wang, L. et al. A review of recent studies on non-resonant piezoelectric actuators. *Mech. Syst. Signal Process.* **133**, 106254 (2019).
10. Yong, Y. K., Aphale, S. S. & Moheimani, S. O. R. Design, Identification, and Control of a Flexure-Based XY Stage for Fast Nanoscale Positioning. *IEEE Trans. Nanotechnol.* **8**, 46–54 (2009).
11. Nagel, W. S., Andersson, S. B., Clayton, G. M. & Leang, K. K. Low-Coupling Hybrid Parallel-Serial-Kinematic Nanopositioner with Nonorthogonal Flexure: Nonlinear Design and Control. *IEEE/ASME Trans. Mechatron.* **27**, 3683–3693 (2022).
12. Barnard, H., Randall, C., Bridges, D. & Hansma, P. K. The long range voice coil atomic force microscope. *Rev. Sci. Instrum.* **83**, 023705 (2012).
13. Liu, Y. et al. Ultra-Large Scale Stitchless AFM: Advancing Nanoscale Characterization and Manipulation with Zero Stitching Error and High Throughput. *Small* **20**, 2303838 (2024).
14. Wang, X. et al. Serial-kinematic hybrid electromagnetic-piezoelectric AFM scanner for high-throughput raster scanning. *IEEE Trans. Ind. Electron.* **72**, 1003–1013 (2025).
15. Tan, L. et al. An electromagnetic-piezoelectric hybrid actuated nanopositioner for atomic force microscopy. *IEEE Trans. Instrum. Meas.* **73**, 7503813 (2024).
16. Li, J., Huang, H. & Morita, T. Stepping piezoelectric actuators with large working stroke for nano-positioning systems: A review. *Sens. Actuators A: Phys.* **292**, 39–51 (2019).
17. Qiao, G. et al. Achieving smooth motion for piezoelectric stick–slip actuator with the inertial block structure. *IEEE Trans. Ind. Electron.* **69**, 3948–3958 (2022).
18. Wang, S. et al. A survey of piezoelectric actuators with long working stroke in recent years: Classifications, principles, connections and distinctions. *Mech. Syst. Signal Process.* **123**, 591–605 (2019).
19. Zhang, S. et al. Piezo robotic hand for motion manipulation from micro to macro. *Nat. Commun.* **14**, 500 (2023).
20. Heaps, E. et al. Bringing real-time traceability to high-speed atomic force microscopy. *Meas. Sci. Technol.* **31**, 074005 (2020).
21. Li, J. et al. Development of a novel parasitic-type piezoelectric actuator. *IEEE/ASME Trans. Mechatron.* **22**, 541–550 (2017).
22. Wang, F. et al. A novel large stepping-stroke actuator based on the bridge-type mechanism with asymmetric stiffness. *Mech. Syst. Signal Process.* **179**, 109317 (2022).
23. Lu, Z. et al. Wafer-scale high-κ dielectrics for two-dimensional circuits via van der Waals integration. *Nat. Commun.* **14**, 2340 (2023).
24. Adams, J. D., Frederix, P. L. T. M. & Bippes, C. A. Breakthrough instruments and products: DriveAFM for high-performance atomic force microscopy. *Rev. Sci. Instrum.* **92**, 129503 (2021).
25. Xu, Z. et al. A stick-slip piezoelectric actuator with high assembly interchangeability. *Int. J. Mech. Sci.* **233**, 107662 (2022).
26. Ma, Z. et al. Piezoelectric-thermal coupling driven biomimetic stick–slip bidirectional rotary actuator for nanomanipulation. *Nano Lett.* **22**, 453–460 (2022).

27. Wang, X., Zhu, L. & Huang, H. A dynamic model of stick-slip piezoelectric actuators considering the deformation of overall system. *IEEE Trans. Ind. Electron.* **68**, 11266–11275 (2021).
28. Huang, H. et al. Achieving stable and effective stick-slip motions of piezoelectric actuators with a small mass rotor by means of the auxiliary friction. *IEEE Trans. Ind. Electron.* **71**, 12835–12845 (2024).
29. Wang, X. et al. Evolution of one-stepping characteristics of a stick-slip piezoelectric actuator under various initial gaps. *Sens. Actuators A: Phys.* **295**, 348–356 (2019).
30. Oubellil, R., Voda, A., Boudaoud, M. & Régnier, S. Mixed stepping/scanning mode control of stick-slip SEM-integrated nano-robotic systems. *Sens. Actuators A: Phys.* **285**, 258–268 (2019).
31. Tian, X., Chen, W., Zhang, B. & Liu, Y. Restraining the backward motion of a piezoelectric stick-slip actuator with a passive damping foot. *IEEE Trans. Ind. Electron.* **69**, 10396–10406 (2022).
32. Lyu, Z. & Xu, Q. Design of a new XY compliant parallel manipulator based on deployable spatial monolithic structucompliant parallel manipulator based on deployable spatial monolithic structu. *IEEE/ASME Trans. Mechatron.* **29**, 3762–3773 (2024).
33. Sang, N. et al. A novel nanopositioning stage integrated with voice coil motor and active eddy current damper. *IEEE/ASME Trans. Mechatron.* **29**, 4411–4422 (2024).
34. Li, J. et al. Development of a Linear Piezoelectric Microactuator Inspired by the Hollowing Art. *IEEE Trans. Ind. Electron.* **69**, 10407–10416 (2022).
35. Schitter, G. et al. Design and modeling of a high-speed AFM-scanner. *IEEE Trans. Control Syst. Technol.* **15**, 906–915 (2007).
36. Wang, K. et al. Multiscale profile characterization based on atomic force Microscopy. *IEEE Trans. Instrum. Meas.* **74**, 1005709 (2025).
37. *Physik Instrumente*, https://www.physikinstrumente.com (2025).
38. *SmarAct*, https://www.smaract.com (2025).
39. *Attocube*, https://www.attocube.com (2025).
40. *Thorlabs*, https://www.thorlabs.com (2025).
41. Wang, F. et al. A novel actuator-internal micro/nano positioning stage with an arch-shape bridge-type amplifier. *IEEE Trans. Ind. Electron.* **66**, 9161–9172 (2019).
42. Kim, G. et al. Binary-state scanning probe microscopy for parallel imaging. *Nat. Commun.* **13**, 1438 (2022).
43. Yong, Y. K., Moheimani, S. O. R., Kenton, B. J. & Leang, K. K. Invited Review Article: High-speed flexure-guided nanopositioning: Mechanical design and control issues. *Rev. Sci. Instrum.* **83**, 121101 (2012).
44. Shan, Y. & Leang, K. K. Accounting for hysteresis in repetitive control design: Nanopositioning example. *Automatica* **48**, 1751–1758 (2012).
45. Nikooienejad, N., Maroufi, M. & Moheimani, S. O. R. Iterative learning control for video-rate atomic force microscopy. *IEEE/ASME Trans. Mechatron.* **26**, 2127–2138 (2021).
46. Suzuki, H. & Wood, R. J. Origami-inspired miniature manipulator for teleoperated microsurgery. *Nat. Mach. Intell.* **2**, 437–446 (2020).
47. Leveziel, M. et al. MiGriBot: A miniature parallel robot with integrated gripping for high-throughput micromanipulation. *Sci. Robot.* **7**, eabn4292 (2022).
48. Gao, X. et al. A compact 2-DOf cross-scale piezoelectric robotic manipulator with adjustable force for biological delicate puncture. *IEEE Trans. Robot.* **40**, 4561–4577 (2024).
49. Albisetti, E. et al. Thermal scanning probe lithography. *Nat. Rev. Methods Prim.* **2**, 32 (2022).
50. Wang, X., Li, L., Zhu, Z. & Zhu, L. Simultaneous damping and tracking control of a normal-stressed electromagnetic actuated nano-positioning stage. *Sens. Actuators A: Phys.* **338**, 113467 (2022).
51. Yang, M. J. et al. High-bandwidth control of nanopositioning stages via an inner-loop delayed position feedback. *IEEE Trans. Autom. Sci. Eng.* **12**, 1357–1368 (2015).

Acknowledgements

The authors would like to thank Dr. Chanmin Su and Dr. Gengliang Chen for the fruitful discussions. The authors would also like to thank Dr. Jiayu Liu for his help during the stitching imaging experiments. This work was supported by the National Key Research and Development Program under Grant No. 2022YFB3403301 (L.Z.), and in part by the National Natural Science Foundation of China under Grant Nos. 52335010 (L.Z.) and U2013211 (L.Z.).

Author contributions

X.W. and L.Z. coordinated and wrote the manuscript; Conceptualization: X.W., L.Z.; Methodology: X.W., Q.Y., J.W.; Investigation: X.W., Q.Y.; Visualization: X.W., Y.M., J.W., H.H.; Funding acquisition: L.Z.; Project administration: L.Z.; Supervision: H.H., L.Z.; Writing – original draft: X.W.; Writing – review & editing: X.W., Q.Y., Y.M., J.W., H.H., L.Z.

Competing interests

The authors declare no competing interests.

Additional information

Supplementary information The online version contains supplementary material available at https://doi.org/10.1038/s41467-025-65579-1.

Correspondence and requests for materials should be addressed to Limin Zhu.

Peer review information *Nature Communications* thanks anonymous reviewer(s) for their contribution to the peer review of this work. A peer review file is available.